BNL-210847-2019-JAAM

Novel manganese-promoted inverse CeO2/CuO catalyst: In situ characterization and activity for the water-gas shift reaction

A. Lopez Camara, J. A. Rodriguez

To be published in "Catalysis Today"

January 2019

Chemistry Department

Brookhaven National Laboratory

U.S. Department of Energy

USDOE Office of Science (SC), Basic Energy Sciences (BES) (SC-22)

DISCLAIMER

Novel manganese-promoted inverse CeO_2/CuO catalyst: In situ characterization and activity for the water-gas shift reaction

A. López Cámara[a], V. Cortés Corberán[a], A. Martínez-Arias[a,*], L. Barrio[b], R. Si[b], J.C. Hanson[b], J.A. Rodriguez[b,*]

[a] *Instituto de Catálisis y Petroleoquímica, CSIC, C/Marie Curie 2, 28049 Madrid, Spain*
[b] *Chemistry Department, Brookhaven National Laboratory, Upton, New York 11973, United States*

Abstract

In this work, the behavior of a novel manganese-promoted inverse CeO_2/CuO catalyst under water-gas shift (WGS) reaction conditions is studied. CeO_2/CuO and CeO_2/Mn-CuO catalysts are characterized by X-ray diffraction (XRD), Raman and X-ray photoelectron spectroscopy (XPS). Structure/activity relationships and redox characteristics are established on the basis of such results along with those of in situ XRD and X-ray absorption fine structure (XAFS) experiments performed either under WGS or CO-temperature programmed reduction (TPR) conditions. The manganese coprecipitated together with the copper during the preparation of the samples and the Mn-CuO phase strongly affected the size and chemical properties of the catalytically-active ceria nanoparticles. A manganese-induced enhancement on the WGS activity was observed. Differences in the characteristics of the supported ceria particles are proposed as most relevant to explain the observed Mn-promoting effect.

Keywords: CeO_2/CuO-Mn, WGS, Hydrogen production, Biomass utilization

[*] Corresponding authors. E-mail: amartinez@icp.csic.es, rodrigez@bnl.gov

Introduction

Molecular hydrogen has been proposed as a potential fuel for motive power and is an essential reactant in many processes of the chemical and petrochemical industries. The water-gas shift (WGS) reaction ($CO + H_2O \rightarrow CO_2 + H_2$) is an important step for hydrogen production from hydrocarbons or other organic compounds [1].Industrial catalysts employed for the process exhibit several shortcomings including low efficiency, deactivation by sintering, high activity only at relatively high operation temperatures as well as the need of strict preconditioning and their high sensitivity to the presence of oxygen or water condensation [1]. This makes them inadequate for on-board application and call for further research and catalyst development.

Catalysts combining copper and cerium oxides have exhibited promising properties in this sense [2,3,4,5,6,7,8,9,10,11]. In contrast with commercial Cu-ZnO-Al_2O_3, the reducibility of ceria in Cu-CeO_2 systems opens the possibility that a bifunctional mechanism, either redox or associative one, operates and enhances their WGS performance [1,3,12,13,14,15]. Accordingly, the specific properties and configuration of both components, copper and cerium oxide, as well as their mutual interaction and interfacial characteristics become most relevant for the optimization of this type of systems [3,12,13,14,16]. In fact, for catalysts combining copper and ceria, as a difference with the commercial catalyst in which the active copper is dispersed on the ZnO-Al_2O_3 support, it is the inverse configuration, i.e. that in which copper oxide (or copper) acts as support of ceria, which has demonstrated optimum properties for the process, thus emphasizing the specific role of the interface in this case [12,16,17]. It appears that the key to the high catalytic activity of such inverse configuration could be related to the nano size of the supported ceria entities as well as the particular interfacial characteristics established in such case [12].

In this context, the present work examines the promoting effect of manganese doping of the CuO component on the WGS activity for the inverse configuration. Such doping should in principle modify the interfacial properties of the catalyst since hopcalite-type materials, mainly based on Cu-Mn mixed oxides, are well known for eliminating CO through oxidation [18,19]. A study and comparison of the doped and undoped catalysts by means of different techniques {X-ray diffraction (XRD), Raman, X-ray photoelectron spectroscopy (XPS), and X-ray absorption fine structure (XAFS)}

provide important insight on the reasons for the mentioned promoting effect on the WGS activity.

Experimental

Inverse catalysts involving CeO_2/(Cu-Mn)O {Cu:Mn nominal atomic ratio of 9:1; Ce:(Cu+Mn) nominal atomic ratio- of 4:6; (Cu9Mn1)6Ce4 in our notation} and CeO_2/CuO {Cu:Cu nominal atomic ratio of 4:6; Cu6Ce4 in our notation} were prepared by employing reverse microemulsions containing n-Heptane, Triton-X-100 and n-Hexanol as organic solvent, surfactant and cosurfactant, respectively, in amounts similar to those reported previously [20]. Full details of the method employed are similar to those employed previously for the preparation of a Zn-doped inverse CeO_2/CuO catalyst, except for the use of Mn instead of Zn, as reported elsewhere [20]. Briefly, the CuO (or Mn-doped CuO) is precipitated first in the microemulsion upon interaction of corresponding nitrate salts of copper (or copper and manganese) with tetramethyl ammonium hydroxide (TMAH) base at mild temperature. Then, cerium is incorporated upon precipitation of cerium nitrate with TMAH. Final treatment consists in calcination under air at 500 ^oC. The samples will be denoted hereafter as Cu6Ce4 and (Cu9Mn1)6Ce4, the numbers reflecting the nominal composition in each case. The same microemulsion procedure was followed for the preparation of a CeO_2 sample employed as a reference for some of the experiments and for which details can be found elsewhere [21]. Chemical analysis of the inverse catalysts, performed by X-ray fluorescence technique, revealed Cu/Ce atomic ratio of 1.547 and 1.304 for Cu6Ce4 and (Cu9Mn1)6Ce4, respectively, close to the nominal values employed; in turn, a Mn/Cu ratio of 0.071, lower than nominal 0.111, was observed. This was attributed to the difficulties for determining the exact number of hydration water molecules present in the initial highly hydrophilic $Mn(NO_3)_2{\cdot}xH_2O$ precursor, taking into account that quantitative precipitation of all components is expected in any case. The specific surface area of the calcined catalysts (as determined by the BET method upon fitting of N_2 adsorption isotherms performed with a Micromeritics 2100 automatic apparatus at liquid nitrogen temperature over catalysts degassed at 140 ^oC for 12 h) was of 98 and 101 m^2g^{-1} for Cu6Ce4 and (Cu9Mn1)6Ce4, respectively.

Time resolved X-ray diffraction (TR-XRD) experiments were carried out on beam line X7B of the National Synchrotron Light Source (NSLS) at BNL with an incident

wavelength of 0.3184 Å. The sample was loaded into a glass cell of 1 mm diameter, attached to a flow system. A small resistance heater was placed just below the capillary, and the temperature was monitored with a 0.1 mm chromel–alumel thermocouple placed in the capillary near the sample. Two dimensional powder patterns were collected with a PerkinElmer amorphous silicon area detector (409.6 mm^2, 2048x2048 pixels and a 200 mm pixel size) and the powder diffraction rings were integrated using the Fit2D code [22]. The instrument parameters (Thompson-Cox-Hastings profile coefficients) were derived from the fit of a LaB_6 reference pattern. Lattice constants were determined by Rietveld analysis. Rietveld profile refinements were performed with the aid of GSAS software [23,24], which allowed for the sequential analysis of phase transitions during the reaction, which was carried out under similar flow conditions as employed for activity tests. The reaction products from TR-XRD experiments were measured with a 0–100 amu quadruple mass spectrometer (QMS, Stanford Research Systems). The samples were analysed in situ under WGS mixture (1% CO, 3% H_2O, in He) or under CO-TPR conditions (5% CO in He with 4 $^oC\ min^{-1}$ ramp).

Cu K-edge time resolved XAFS spectra (TR-XAFS) were collected at beamline X18A of the NSLS under similar operational conditions as those employed for the TR-XRD experiments. The same cell was used for the XAFS experiments as that for TR-XRD, except that the sample was loaded into a Kapton capillary and heated with a hot air blower. The X-ray absorption spectra were taken repeatedly in the ‘‘fluorescence-yield mode’’ using a passivated implanted planar silicon (PIPS) detector cooled with circulating water. The XAFS data were then analyzed using the Athena software [25].

Raman spectra were obtained at room temperature (RT) with a Bruker RFS-100 FT-Raman spectrometer provided with a diode-pumped germanium solid-state detector, which operates at liquid nitrogen temperature. A NdYAG laser (1064 nm) was used as excitation source at a power of 100 mW. Powdered samples were pressed in a holder and analyzed (100 scans, 4 cm^{-1} resolution) without further treatment.

X-ray photoelectron spectra (XPS) were collected utilizing a Specs Gmbh spectrometer under UHV conditions ($P \approx 10^{-10}$ mbar) and using Mg Kα radiation and a Phoibos 1509MCD energy analyzer. During data processing of the XPS spectra, the binding energy values were estimated by using as reference the C 1s peak of contaminant carbon at 285.0 eV; correct correction was further checked by adjusting the

characteristic u”’ peak of Ce 3d to 917.0 eV [26]. The Casa XPS software package was used for data analysis.

The WGS reaction activity test was carried out using a fixed-bed reactor system from PID Eng&Tech (model Microactivity Reference) at atmospheric pressure. 1 g of calcined catalyst (diluted with 4 g of CSi) was positioned inside the 9 mm i.d. Hastelloy C reactor. Prior to reaction, the catalyst was calcined in situ in a 20% O_2/He gas mixture at 500 ^oC for 1 h. The reactant gas mixture consisted of 5 % CO and 15 % H_2O diluted in He. Distilled water was dosed by means of a Gilson 307 HPLC pump and evaporated in a heat box, operating at 180 ^oC, which is integrated in the reactor system. The total reactant flow was 250 cm^3 min^{-1} (STP), which corresponds to GHSV of ca. 15.000 h^{-1}. The analysis of the outlet flow was made under apparent steady state conditions (temperature stabilized over, at least, 45 minutes) every 50 ^oC from 200 to 500 ^oC. Reaction products and remaining reactants were efficiently separated by means of capillary columns, and qualitatively and quantitatively analyzed with a Shimazdu gas chromatograph equipped with a TCD detector. The transfer line between the reactor system and gas chromatograph was heated to 190 ^oC using a heating tape in order to prevent water vapor condensation and to ensure acquisition of reliable data.

Results and discussion

Characterization of the catalysts. X-ray diffractograms for the Cu6Ce4 and (Cu9Mn1)6Ce4 catalysts are shown in Figure 1. They appear very similar to each other and only exhibit peaks attributable to the fluorite phase of CeO_2 and the tenorite phase of CuO. No peak attributable to segregated Mn-containing phases is observed in (Cu9Mn1)6Ce4. The results of Rietveld analysis of these diffractograms are shown in Table 1. Crystal size was estimated using the Scherrer equation [23,24]. The two catalysts are composed of small crystals of cerium oxide (between ca. 4 and 5 nm) and larger particles of copper oxide (around 20 nm). The doping of the catalyst with manganese leads to a decrease in the crystal size of both components, particularly important in the case of the CeO_2 phase (Table 1). It also worth mentioning that the molar ratio of CuO to CeO_2 obtained by X-ray diffraction (based on the Rietveld quantification of CuO vs. CeO_2) is significantly lower than expected from chemical composition values (see Experimental) for both catalysts; this difference is more pronounced for the Mn-containing catalyst. This suggests that in any case an

appreciable amount of the copper forms amorphous entities, in a more pronounced way for (Cu9Mn1)6Ce4.

The structural analysis was complemented by Raman spectroscopy. Figure 2 displays the spectra obtained for the two catalysts as well as that for a CeO_2 reference prepared under similar conditions. In all cases a band is observed around 460 cm^{-1}, corresponding to the triple degenerate vibrational mode F_{2g} of the fluorite structure (face-centered cubic) of the ceria, for which this band corresponding to the first-order transition is the only one allowed for a perfect crystal [27]. It is observed a very strong decrease in the intensity of this peak in the inverse catalysts with respect to the CeO_2 reference. This effect may be due, on the basis of UV-Vis results in this type of systems [28], to a great increase in optical absorption when copper is present in the system. This effect can also limit the sampling depth of the exploration, making more difficult to get information from the bulk of the sample [29]. It is also observed that the band around 460 cm^{-1} shows a slight red shift with respect to that in the CeO_2 reference. Along with this, a broad band around 600 cm^{-1}, related to the presence of lattice defects (oxide anions either in the environment of an oxygen vacancy and/or interstitial ones) [27,30,31]. This band could arise as a consequence of a certain degree of ceria reduction (necessarily accompanied by formation of oxygen vacancies to keep lattice neutrality), which is favored for CeO_2 crystals of a few nanometers in size [27,32], as it occurs for the two inverse catalysts (Table 1). In this sense, it should be noted that, according to the data collected in Table 1, the lattice parameter of the fluorite phase in the inverse samples is slightly higher than expected for pure CeO_2 (5.411 Å), as expected when the sample presents a certain reduction degree. Nevertheless, we cannot discard that some amount of copper or manganese heterocations could be inserted in the ceria lattice, which could also lead to similar effects [21]. In addition, two peaks are observed at about 296 and 350 cm^{-1}, corresponding to the presence of the tenorite phase of copper oxide [33], a third band around 620 cm^{-1} would also be expected for this phase, note however it appears as an overlapped shoulder over the wide band associated with defective oxygens in the ceria phase. These bands practically disappear or become strongly broadened when the catalyst is doped with Mn. This is in line with an increase in the amount of amorphous material in the copper oxide phase of this catalyst and correlates with the analysis of the XRD results presented above, as well as with the fact that the manganese is coprecipitated together with the copper during the preparation of the sample and therefore strongly affects the copper oxide phase.

Characterization of the surface layers of the initial calcined catalysts has been performed by XPS. Figure 3 displays the spectra obtained in most relevant regions. The spectra in the Ce 3d region show a set of two doublets which correspond to a deconvolution into eight peaks labelled as u (u-u''') for $3d_{3/2}$ and v (v-v''') for $3d_{5/2}$. Among them, the doublet v'/ u' is considered as the fingerprint of the presence of Ce^{3+} (note this is only a practical simplification since it corresponds only to the center of most intense peak among the set of peaks observed for Ce_2O_3 [34]) whereas the other peaks are attributed to Ce^{4+} [26,34]. According to the relative contribution of the Ce^{3+} features to the spectrum, 15.6 and 18.6% of the cerium appears as Ce^{3+} in Cu6Ce4 and (Cu9Mn1)6Ce4, respectively, as collected in Table 2. The relatively higher amount of Ce^{3+} in the latter can be due to the lower crystal size observed for it (Table 1), as discussed above. Concerning the O 1s region, basically two peaks are observed for the two samples at 532.0 and 530.4 eV. The peak at 530.4 corresponds to bulk oxygens either from CeO_2 or CuO components [35]. The peak at 532.0 eV is typical for oxygens from chemisorbed or surface species like hydroxyls or carbonates difficult to eliminate during steps of precursor decomposition involved in the preparation and/or as a consequence of interaction with atmospheric air [35]. No important difference appears between the spectra of the two samples in this O 1s region.

In the Cu 2p3/2 region, the spectra are basically constituted by two main peaks at ca. 934.0 and 935.8 eV. The two peaks, along with satellite peaks appearing in the 947-938 eV region, can correspond to Cu^{2+} species in oxidic and oxy-hydroxidic environments, respectively [35,36,37]. The latter correlates well with the important intensity observed for oxygen in hydroxyls in the O1s region, as described above. However, the ratio of intensities between satellite and main peaks (Table 2) appears well below expected value for pure CuO (around 0.55 [38]), indicating that an appreciable part of the copper appears probably as Cu^{+} in both samples, the corresponding contribution probably appearing overlapped in the peak at 934.0 eV. Use of corresponding Cu_{LMM} Auger peak (not shown) does not unfortunately help to get more details in this respect; in both cases, a broad peak with maximum around 917.8 eV, close to that shown by CuO [39], is observed and suggests on the whole that most of the copper is in a Cu^{2+} state in both samples. It can be noted that no peak for Cu^{+} species around 931.0 eV is detected for (Cu9Mn1)6Ce4; such peak is characteristic for Cu^{+} species in the tetrahedral position of the $CuMn_2O_4$ spinel [40,41], most stable mixed oxide compound between Cu and Mn [40], thus suggesting that such type of

compound is not formed. In turn, the Mn 2p spectra reveal the presence of two 2p3/2 contributions at 642.5 and 645.0 eV which can be assigned to Mn^{2+} (along with possibly minor satellite peak at ca. 648 eV, not considered during fitting due to overlapping with the broad high BE peak) and Mn^{4+} species, respectively [41,42].

Finally, Table 2 collects relevant atomic ratio values determined from the intensity of the XPS peaks, corrected with adequate sensitivity factors [43]. A first one ([Ce]/([Ce]+[Cu]+[Mn])) is related with the relative dispersion of the CeO_2 as supported phase employed in the two examined catalysts. It is noted that this ratio is slightly lower in (Cu9Mn1)6Ce4. This is in contrast with the lower crystal size observed for the supported CeO_2 particles in this sample and taking into account that it is the structure of such supported phase which is expected to determine the textural properties of this type of samples [41]. However, one should bear in mind that the CeO_2 crystals typically organize in the form of agglomerates over the surface of copper oxide [20,44], previous high resolution electron microscopy images for Cu6Ce4 are available and demonstrate this [20]. It appears therefore that the degree of agglomeration of the ceria nanocrystals is higher for (Cu9Mn1)6Ce4. This could also explain the fairly similar specific surface area exhibited by the two samples, despite the important difference in CeO_2 crystal size (Experimental and Table 1). On the other hand, the [Mn]/([Mn]+[Cu]) atomic ratio observed for (Cu9Mn1)6Ce4 evidences certain surface enrichment in manganese for this sample, taking into account its chemical composition (Experimental).

Catalytic and redox properties. Figure 4 shows the WGS activity observed over the Cu6Ce4 and (Cu9Mn1)6Ce4 catalysts. The (Cu9Mn1)6Ce4 system is shown to be more active than Cu6Ce4. It reaches more than 70% CO conversion at 200 ^oC at which Cu6Ce4 shows 60% conversion. Differences become lower as the reaction temperature becomes higher while equilibrium conditions are achieved above 300 and 325 ^oC for (Cu9Mn1)6Ce4 and Cu6Ce4, respectively. In any case, the promoting effect of the presence of manganese on the WGS activity appears evident. These differences in activity did not change after several cycles of catalyst use.

In order to explain such a promoting effect, the catalysts were examined by TR-XRD under WGS reaction conditions. The evolution of the different phases observed in the diffractograms as a function of time/temperature for the two examined catalysts is shown in Figure 5. The catalysts start from oxidized states in both components, as discussed above (Fig. 1), and evolve to reduced states during the course of the run. Concerning the copper component, the original tenorite CuO phase becomes

transformed, first to Cu_2O and finally to metallic copper, during the course of the heating under the WGS mixture up to 200 ºC. The main difference between the two catalysts for such component is related to a somewhat lower reducibility of the copper for (Cu9Mn1)6Ce4. Thus, first reduction to Cu_2O starts a little before for Cu6Ce4 while full reduction to metallic copper is accomplished also in a faster way over this catalyst and the reduction of the Cu_2O intermediate appears also slower in (Cu9Mn1)6Ce4. In turn, the CeO_2 component becomes concomitantly reduced. This is based on the expansion observed in corresponding lattice parameter, taking into account that the reduction of CeO_2 implies the lattice expansion as a consequence of formation of Ce^{3+} and oxygen vacancies [27,32,45], as represented in Fig. 5. Up to ca. 15 min., the observed increase is attributed to thermal expansion; note about 0.15 Å shift is expected as a consequence of such expansion from 25 to 200 ºC [45]. Then, simultaneous to the reduction of CuO to Cu_2O, reduction of the ceria component is revealed by the increase observed in lattice parameter which apparently exceeds the linear increase expected for simple thermal expansion. A more important increase in the lattice parameter, and therefore a higher reduction level, is then observed simultaneous to the reduction of the copper component to metallic copper. The main difference between the two samples for such reduction process is related to the respective degree of reduction achieved in the ceria nanoparticles. This is higher for (Cu9Mn1)6Ce4 where an expansion of 0.037 Å is observed up to 200 ºC while Cu6Ce4 expands to 0.035 Å. In turn, the analysis of gases evolution (Fig. 5) reveals that the reduction of the samples takes place as a consequence of interaction with CO with consequent CO_2 production while WGS activity, revealed by the increase in the m/e = 2 MS signal corresponding to H_2, only starts when copper reduction becomes practically complete.

Similar trends are observed when analyzing the reduction of the systems under CO, as shown in Figure 6. Thus, copper appears less reducible in (Cu9Mn1)6Ce4. In both catalysts, as a difference with the experiments in the presence of H_2O (Fig. 5), CuO is practically reduced to metallic copper without practical formation of intermediate Cu_2O during the reduction process. Such reduction takes place in practically one step for Cu6Ce4 (reduction maximum at ca. 125 ºC) while it appears more complex since it takes place in two separated steps with maxima at ca. 150 and 190 ºC, for (Cu9Mn1)6Ce4. Such complexity is probably a consequence of heterogeneities associated to the presence of manganese in the catalyst. In any case, the lower reducibility of the copper in (Cu9Mn1)6Ce4 is revealed by the slightly higher

temperature at which CuO reduction starts as well as the fact that such reduction proceeds in an apparently slower way, full reduction to metallic copper being achieved at appreciably higher temperature. In contrast, as it occurred under the WGS reaction mixture, the level of reduction achieved for the ceria component appears larger for (Cu9Mn1)6Ce4, as revealed by the higher shift observed in the evolution of the lattice parameter during the run.

Since XRD characterization of (Cu9Mn1)6Ce4 revealed that an appreciable part of the copper in the initial calcined sample was present in the form of amorphous entities not detected by XRD, this catalyst has been examined by XAFS in the Cu K-edge, as shown in Figure 7. The starting calcined sample presents a state which appears quite similar to that of the CuO reference and in which most of the copper appears as Cu^{2+}. In agreement with XRD results (Fig. 5), the sample evolves towards reduced states upon increasing the temperature under the WGS mixture. Further than small differences in the temperature at which the reduction process takes place in every case, which is related to differences in respective type of experimental set-ups employed, the evolution of copper state appears fairly similar in both types of experiments (XRD and XAFS, Figs. 5 and 7, respectively). Thus, according to the XAFS investigation, the initial oxidized state (Cu^{2+}) is kept up to ca. 180 ºC where the sample begins a reduction process, first to Cu^{+} and then, immediately after, to metallic copper with the Cu^{+} state becoming partially stabilized at intermediate temperature.

Structure/activity relationship. WGS activity over catalysts combining copper and cerium oxides has been related to the properties of the interfaces established between the two components and in which active sites are proposed to be located [3,11,12,13,14,16,17,46]. These have been proposed to involve both metallic copper and oxygen vacancies in ceria, thus emphasizing the interfacial character of the process [3]. Discussion still exists with respect to the type of mechanism operating, either redox or associative one (or both, depending on the reaction temperature), in which the interfacial sites are involved in any case, as discussed in detail elsewhere [16]. The involvement of metallic copper and reduced cerium entities (or oxygen vacancies in their close environment) as active sites is in agreement with the results presented in Fig. 5 in which the WGS activity is shown to trigger only in the presence of such type of species. Taking into account the interfacial character of the process, a first hypothesis to explain the higher activity of (Cu9Mn1)6Ce4 would be the fact that a higher amount of interfacial sites is present in this catalyst. This follows from the fact that this catalyst

presents lower size in the supported ceria particles and therefore a higher degree of ceria dispersion on the copper oxide support could be expected. However, as mentioned above, it must be taken into account that the ceria nanoparticles do not appear as isolated entities dispersed on the support but they form aggregates. In this sense, as discussed above, the XPS results (Fig. 3 and Table 2) do not support a higher ceria dispersion in (Cu9Mn1)6Ce4 but rather, most likely as a consequence of respective degree of agglomeration of the ceria particles, this would finally present poorer dispersion than Cu6Ce4. Then, the highest activity of (Cu9Mn1)6Ce4 must not be attributed to the presence of a higher amount of interfacial active sites in it.

Rather, the results point to a higher intrinsic activity of the active sites present in (Cu9Mn1)6Ce4. The presence of manganese in this catalyst apparently decreases the reducibility of the copper oxide phase both under WGS conditions (Fig. 5) or under pure CO (Fig. 6). According to results in the scientific literature, promoting effects of manganese on copper WGS activity are typically of an indirect character and related to the enhancement of copper dispersion or reducibility [47,48]. In the case of (Cu9Mn1)6Ce4, as discussed above, no evidence of mixed oxide Cu-Mn spinel formation is found and in principle any effect of manganese on the copper oxide properties would also be of an indirect character and as a consequence of the interaction of copper with dispersed manganese oxide entities. On the other hand, correlation between WGS activity and copper reducibility has been also pointed out [48,49,50,51]. Therefore, the fact that manganese decreases the reducibility of copper in (Cu9Mn1)6Ce4 (Figs. 5 and 6) does not point towards this effect as responsible of the observed enhancement in WGS activity for this catalyst (Fig. 4). In contrast, the ceria component displays higher reducibility in (Cu9Mn1)6Ce4 (Figs. 5 and 6), as discussed above. This can explain the higher WGS activity observed for this system (Fig. 4). Thus, if a redox mechanism operates, a higher level of reduction in the ceria component will increase the H_2O dissociation activity, considered as rate determining step [12,46], during the step of surface oxidation. In turn, the mentioned associative mechanism can be also enhanced when the ceria component becomes more reduced [13,14]. Therefore, the promotion of WGS activity observed for (Cu9Mn1)6Ce4 can be related to the lower size of the supported ceria particles formed when manganese is present in the catalyst; according to the characterization results, it cannot be discarded some role of heterocationic (copper and/or manganese) modification of the ceria fluorite phase. The important role of the supported ceria particles on the WGS activity of this type of

catalysts was already pointed out during studies of gold or copper model systems in which the direct participation of the deposited ceria nanoparticles on the activity was demonstrated [16,52].

Conclusions

Introduction of manganese as a dopant in the copper oxide phase during the preparation of an inverse CeO_2/CuO catalyst enhances its WGS activity. Characterization of the Mn-containing catalyst in comparison with its analogous Mn-free system reveals differences which affect mainly the supported ceria particles. These display lower crystal size while they can be more affected by the presence of heterocations (copper and/or manganese) in their structure for the manganese-containing catalyst. Despite the lower crystal size of the supported ceria particles in the Mn-containing catalyst, XPS results do not point towards a higher dispersion of cerium in it, which is attributed to differences in respective degree of agglomeration of the ceria nanoparticles in each case. This means that the enhanced WGS activity of the Mn-containing catalyst cannot be attributed to the presence of a higher amount of interfacial active sites in it. Rather, the results point towards a higher intrinsic activity of the active sites in this catalyst. In this sense, the difference in the characteristics of the supported ceria particles is proposed as most relevant to explain the observed promoting effect on the WGS activity. This is based on the comparative analysis of the two catalysts by means of in situ-XRD or –XAFS either under WGS reaction conditions or during CO-TPR examination. While the presence of manganese hinders to a certain extent the reduction of copper in the catalyst, an increase of the reduction level in the supported ceria particles is produced. This can favour water activation and/or generation of active intermediates leading to enhanced WGS activity. Therefore, as the main conclusion and in agreement with previous studies on model systems [52], the results evidence that, among the two components of this type of catalysts, it is the characteristics of the ceria nanoparticles which mainly determine the WGS catalytic properties of catalysts combining copper and CeO_2.

Acknowledgements

The Ministerio de Economía, Industria y Competitividad is acknowledged for financial support (project CTQ2015-71283-R). The work carried out at Brookhaven National Laboratory was supported by the U.S. Department of Energy (Chemical Sciences Division, DE-SC0012704). The help provided by Dr. G. Zhou during measurements at the NSLS beamline X7B is greatly acknowledged.

References

[1] C. Ratnasamy, J.P. Wagner. Water gas shift catalysis. Catal. Rev. Sci. Eng. 51 (2009) 325-440.

[2] Y. Li, Q. Fu, M. Flytzani-Stephanopoulos. Low-temperature water-gas shift reaction over Cu- and Ni-loaded cerium oxide catalysts. Appl. Catal. B 27 (2000) 179-191.

[3] X. Wang, J.A. Rodriguez, J.C. Hanson, D. Gamarra, A. Martínez-Arias, M. Fernández-García. In situ studies of the active sites for the water gas shift reaction over Cu-CeO_2 catalysts: complex interaction between metallic copper and oxygen vacancies of ceria. J. Phys. Chem. B 110 (2006) 428-434.

[4] H. Kusar, S. Hocevar, J. Levec. Kinetics of the water-gas shift reaction over nanostructured copper-ceria catalysts. Appl. Catal. B 63 (2006) 194-200.

[5] A.S. Quiney, Y. Schuurman. Kinetic modeling of CO conversion over a Cu/CeO2 catalyst. Chem Eng. Sci. 62 (2007) 5026-5032.

[6] T. Tabakova, V. Idakiev, J, Papavasiliou, G. Avgoropoulos, T. Ioannides. Effect of additives on the WGS activity of combustion synthesized CuO/CeO_2 catalysts. Catal. Commun. 8 (2007) 101-106.

[7] P. Djinovic, J. Batista, J. Levec, A. Pintar. Comparison of water-gas shift reaction activity and long-term stability of nanostructured CuO-CeO_2 catalysts prepared by hard template and co-precipitation methods. Appl. Catal. A 364 (2009) 156-165.

[8] P.V.D.S.Gunawardana, H.C Lee, D.H. Kim. Performance of copper-ceria catalysts for water-gas shift reaction in medium temperature range. Int. J. Hydr. Ener. 34 (2009) 1336-1341.

[9] P. Gawade, B. Mirkelamoglu, U.S. Ozkan. The Role of Support Morphology and Impregnation Medium on the Water Gas Shift Activity of Ceria-Supported Copper Catalysts. J. Phys. Chem. C 114 (2010) 18173-18181.

[10] J. Kugai, J.T. Miller, N. Guo, C. Song. Oxygen-enhanced water gas shift on ceria-supported Pd-Cu and Pt-Cu bimetallic catalysts. J. Catal. 277 (2011) 46-53.

[11] S.Y. Yao, W.Q. Xu, A.C. Johnston-Peck, F.Z. Zhao, Z.Y. Liu, S. Luo, S.D. Senanayake, A. Martínez-Arias, W.J. Liu, J. A. Rodriguez. Morphological effects of the nanostructured ceria support on the activity and stability of CuO/CeO_2 catalysts for the water-gas shift reaction. Phys. Chem. Chem. Phys. 16 (2014) 17183-17195.

[12] J.A. Rodriguez, J. Graciani, J. Evans, J.B. Park, F. Yang, D. Stacchiola, S.D. Senanayake, S. Ma, M. Pérez, P. Liu, J.F.. Sanz, J. Hrbek. Water-Gas Shift Reaction on a Highly Active Inverse CeO_x/Cu(111) Catalyst: Unique Role of Ceria Nanoparticles. Angew. Chem. Int. Ed.48 (2009) 8047 –8050.

[13] K. Mudiyanselage, S.D. Senanayake, L. Feria, S. Kundu, A-E. Baber, J. Graciani, A.B. Vidal, S. Agnoli, J. Evans, R. Chang, S. Axnanda, Z. Liu, J.F. Sanz, P. Liu, J.A. Rodriguez, D.J. Stacchiola. Importance of the metal-oxide interface in catalysis: in situ studies of the water-gas shift reaction by ambient-pressure X-ray photoelectron spectroscopy. Angew. Chem. Int. Ed. 52 (2013) 5101 –5105.

[14] J. Graciani, J.F. Sanz. Designing a new generation of catalysts: Water gas shift reaction example. Catal. Today 240 (2015) 214-219.

[15] A. López Cámara, S. Chansai, C. Hardacre, A. Martínez-Arias. The water-gas shift reaction over CeO_2/CuO : Operando SSITKA-DRIFTS-mass spectrometry study of low temperature mechanism. Int. J. Hydr. Ener. 39 (2014) 4095-4101.

[16] A. Kubacka, A. Martínez-Arias, M. Fernández-García. Role of the Interface in Base-Metal Ceria-Based Catalysts for Hydrogen Purification and Production Processes. ChemCatChem 7 (2015) 3614-3624.

[17] L. Barrio, M. Estrella, G. Zhou, W. Wen, J.C. Hanson, A.B. Hungría, A. Hornés, M. Fernández-García, A. Martínez-Arias, J.A. Rodriguez. Unraveling the Active Site in Copper-Ceria Systems for the Water-Gas Shift Reaction: In Situ Characterization of an Inverse Powder CeO_{2-x}/CuO−Cu Catalyst. J. Phys. Chem. C 114 (2010) 3580–3587.

[18] T.H. Rogers, C.S. Piggot, W.H. Bahlke, J.M. Jennings. The Catalytic Oxidation of Carbon Monoxide. J. Am. Chem. Soc. 43 (1921) 1973-1982.

[19] D.R. Merrill, C.C. Scalione. The Catalytic Oxidation of Carbon Monoxide at Ordinary Temperatures. J. Am. Chem. Soc. 43 (1921) 1982-2002.

[20] A. López Cámara, V. Cortés Corberán, L. Barrio, G. Zhou, R. Si, J. C. Hanson, M. Monte, J.C. Conesa, J.A. Rodriguez, A. Martínez-Arias. Improving the CO-PROX Performance of Inverse CeO_2/CuO Catalysts: Doping of the CuO Component with Zn. J. Phys. Chem. C 118 (2014) 9030-9041.

[21] D. Gamarra, G. Munuera, A.B. Hungría, M. Fernández-García, J.C. Conesa, P.A.Midgley, X.Q. Wang, J.C. Hanson, J.A. Rodriguez, A. Martínez-Arias. Structure-Activity Relationship in Nanostructured Copper-Ceria-Based Preferential CO Oxidation Catalysts. J. Phys.Chem. C 111 (2007) 11026–11038.

[22]:A.P. Hammersley. *FIT2D An Introduction and Overview*; ESRF Internal Report ESRF97HA02T, Grenoble, France; 1997.

[23] B.H. Toby. EXPGUI, a graphical user interface for GSAS. J. Appl. Crystal. 34 (2001) 210-213**.**

[24] A.C. Larson, R.B. von Dreele,. GSAS General Structure Analysis System. Report LAUR 86-748, Los Alamos National Laboratory: Los Alamos, NM, 1995.

[25] (a) M. Newville, B. Ravel, D. Haskel, J.J. Rehr, E.A. Stern, Y. Yacoby. Analysis of multiple-scattering XAFS data using theoretical standards. Physica B, 208-209 (1995), 154-156. (b) B. Ravel, M.J. Newville. ATHENA, ARTEMIS, HEPHAESTUS: data analysis for X-ray absorption spectroscopy using IFEFFIT. J. Synchr. Rad. 12 (2005) 537-541.

[26] A. Martínez-Arias, M. Fernández-García, A.B. Hungría, J.C. Conesa, G. Munuera. Spectroscopic Characterization of Heterogeneity and Redox Effects in Zirconium−Cerium (1:1) Mixed Oxides Prepared by Microemulsion Methods. J. Phys. Chem. B 107 (2003) 2667-2677.

[27] J.E. Spanier, R.D. Robinson, F.Zhang, S.W. Chan, I.P. Herman. Size-dependent properties of CeO_{2-y} nanoparticles as studied by Raman scattering. Phys. Rev. B. 64 (2001) 245407/1-8..

[28] W. Shan, W. Shen, C. Li. Structural Characteristics and Redox Behaviors of $Ce_{1-x}Cu_xO_y$ Solid Solutions. Chem. Mater. 15 (2003) 4761-4767.

[29] M.-F. Luo, Z.-L. Yan, L.-Y. Jin, M. He. Raman Spectroscopic Study on the Structure in the Surface and the Bulk Shell of $Ce_xPr_{1-x}O_{2-\delta}$ Mixed Oxides. J. Phys. Chem. B 110 (2006) 13068-13071.

[30] Z. Wu, M. Li, J. Howe, H.M. Meyer, S.H. Overbury. Probing defect sites on CeO_2 nanocrystals with well-defined surface planes by Raman spectroscopy and O_2 adsorption. Langmuir 26 (2010) 16595-16606.

[31] L. Ilieva, P. Petrova, G. Pantaleo, R. Zanella, L.F. Liotta, V. Georgiev, S. Boghosian, Z. Kaszkur, J.W. Sobczak, W. Lisowski, A.M. Venezia, T. Tabakova. Gold

catalysts supported on Y-modified ceria for CO-free hydrogen production via PROX. Appl. Catal. B 188 (2016) 154-168.

[32] M. Fernández-García, A. Martínez-Arias, J.C. Hanson, J.A. Rodriguez. Nanostructured oxides in chemistry: characterization and properties. Chem. Rev. 104 (2004) 4063-4104.

[33] J.F. Xu, W. Ji, Z.X. Shen, W.S. Li, S.H. Tang, R.X. Ye, D.Z. Jia, X.Q. Xin. Raman Spectra of CuO Nanocrystals. J. Raman Spectrosc. 30 (1994) 413-415.

[34] J.P. Holgado, R. Alvarez, G. Munuera. Study of CeO_2 XPS spectra by factor analysis: reduction of CeO_2. Appl. Surf. Sci. 161 (2000) 301-315.

[35] M. Monte, G. Munuera, D. Costa, J.C. Conesa, A. Martínez-Arias. Near-ambient XPS characterization of interfacial copper species in ceria-supported copper catalysts. Phys. Chem. Chem. Phys. 17 (2015) 29995-30004.

[36] A. Martínez-Arias, A.B. Hungría, M. Fernández-García, A. Iglesias-Juez, J. Soria, J.C. Conesa, J.A. Anderson, G. Munuera. Operando DRIFTS study of the redox and catalytic properties of $CuO/Ce_{1-x}Tb_xO_{2-\delta}$ (x = 0-0.5) catalysts: evidence of an induction step during CO oxidation. Phys. Chem. Chem. Phys. 14 (2012) 2144-2151.

[37] I. Platzman, R. Brener, H. Haick, R. Tannenbaum. Oxidation of Polycrystalline Copper Thin Films at Ambient Conditions. J. Phys. Chem. C 112 (2008) 1101-1108.

[38] J. Ghijsen, L.H. Tjeng, J. van Elp, H. Eskes, J. Westerink, G.A. Sawatzky, M.T. Czyzyk. Electronic structure of Cu_2O and CuO. Phys. Rev. B 38 (1988) 11322-11330.

[39] D.A. Svintsitskiy, T.Y. Kardash, O.A. Stonkus, E.M. Slavinskaya, A.I. Stadnichenko, S.V. Koscheev, A.P. Chupakhin, A.I. Boronin. In Situ XRD, XPS, TEM, and TPR Study of Highly Active in CO Oxidation CuO Nanopowders. J. Phys. Chem. C 117 (2013) 14588-14599.

[40] B. Gillot, S. Buguet, E. Kester. Oxidation mechanism and valence states of copper and manganese in tetragonal $CuMn_2O_4$. J. Mater. Chem. 7 (1997) 2513-2517

[41] A. Elmhamdi, L. Pascual, K. Nahdi, A. Martínez-Arias. Structure/redox/activity relationships in $CeO_2/CuMn_2O_4$ CO-PROX catalysts. Appl. Catal. B 217 (2017) 1-11.

[42] B.R. Stromheimer, D.M. Hercules. Surface spectroscopic characterization of manganese/aluminum oxide catalysts. J. Phys. Chem. 88 (1984) 4922-4929.

[43] C.D. Wagner, L.E. Davis, M.V. Zeller, J.A. Taylor, R.H.Raymond, L.H. Gale. Empirical atomic sensitivity factors for quantitative-analysis by electron-spectroscopy for chemical-analysis. Surf. Interf. Anal. 3 (1981) 211-225.

[44] A. Hornés, A.B. Hungría, P. Bera, A. López Cámara, M. Fernández-García, A. Martínez-Arias, L. Barrio, M. Estrella, G. Zhou, J.A. Fonseca, J. Hanson, J.A. Rodriguez. Inverse CeO_2/CuO Catalyst As an Alternative to Classical Direct Configurations for Preferential Oxidation of CO in Hydrogen-Rich Stream. J. Am. Chem. Soc. 132 (2010) 34-35.

[45] J.A. Rodriguez, J.C. Hanson, J.-Y. Kim, G. Liu, A. Iglesias-Juez, M. Fernández-García. Properties of CeO_2 and $Ce_{1-x}Zr_xO_2$ Nanoparticles: X-ray Absorption Near-Edge Spectroscopy, Density Functional, and Time-Resolved X-ray Diffraction Studies. J. Phys. Chem. B 107 (2003) 3535-3543.

[46] A. Kubacka, M. Fernández-García, A. Martínez-Arias. Catalytic hydrogen production through WGS or steam reforming of alcohols over Cu, Ni and Co catalysts. Appl. Catal. A 518 (2016) 217.

[47] T. Tabakova, V. Idakiev, G. Avgouropoulos, J. Papavasiliou, M. Manzoli, F. Boccuzzi, T. Ioannides. Highly active copper catalyst for low-temperature water-gas shift reaction prepared via a Cu-Mn spinel oxide precursor. Appl. Catal. A 451 (2013) 184-191

[48] C. Li, Z. Li, H.Y. Oh, G.H. Hong, J.S. Park, J.M. Kim. Ordered mesoporous Cu-Mn-Ce ternary metal oxide catalysts for low temperature water-gas shift reaction. Catal. Today 307 (2018) 237-242

[49] L. Li, L. Song, C. Chen, Y. Zhang, Y. Zhan, X. Lin, Q. Zheng, H. Wang, H. Ma, L. Ding, W. Zhu. Modified precipitation processes and optimized copper content of CuO-CeO_2 catalysts for water-gas shift reaction. Int. J. Hydr. Ener. 39 (2014) 19570-19582.

[50] D.-W. Jeong, W.-J. Jang, J.-O. Shim, W.-B. Han, H.-S. Roh, U.H. Jung, W.L. Yoon. Low-temperature water-gas shift reaction over supported Cu catalysts. Renew. Ener. 65 (2014) 102-107

[51] L. Li , L. Song, H. Wang, C. Chen, Y. She, Y. Zhan, X. Lin, Q. Zheng. Water-gas shift reaction over CuO/CeO_2 catalysts: Effect of CeO_2 supports previously prepared by precipitation with different precipitants. Int. J. Hydr. Ener. 36 (2011) 8839-8849

[52] J.A. Rodriguez, S. Ma, P. Liu,; J. Hrbek, J. Evans, M. Perez. Activity of CeO_x and TiO_x nanoparticles grown on Au(111) in the water–gas shift reaction. Science 318 (2013) 1757-1760.

Table 1. Main structural properties of the catalysts, as determined by Rietveld analysis of the X-ray diffractograms shown in Fig.1.

Catalyst	CeO_2 crystal size (nm)	CuO crystal size (nm)	CeO_2 lattice parameters (Å)	CuO lattice parameters (Å)	$[CuO]/[CeO_2]$[a]
Cu6Ce4	4,9	20,1	5,421	a = 4,680 b = 3,441 c = 5,133	1.25
(Cu9Mn1)6Ce4	3,9	18,7	5,419	a = 4,688 b = 3,432 c = 5,136	0.91

[a] Ratio determined from quantification of peaks corresponding to the indicated phases

Table 2. Atomic ratios extracted from analysis of the XPS results.

Catalyst	$[Ce^{3+}]/[Ce_{total}]$	ICu_{sat}/ICu_{main}	[Ce]/([Ce]+[Cu]+[Mn])	[Mn]/([Mn]+[Cu])
Cu6Ce4	15.6%	0.24	0.56	
(Cu9Mn1)6Ce4	18.6%	0.27	0.50	0.17

Figure captions

Figure 1. X-ray diffractograms for the indicated catalysts. Marks for the observed phases are indicated.

Figure 2. Raman spectra for the indicated samples. A CeO_2 reference is included for comparative purpose (see main text).

Figure 3. XPS spectra of the indicated initial calcined samples in regions Ce3d (top left), $Cu2p_{3/2}$ (top right), O1s (bottom left) and $Mn2p_{3/2}$ (bottom right).

Figure 4. CO conversion during the WGS reaction (5% CO + 15% H_2O in He) over the indicated catalysts.

Figure 5. Bottom: evolution of the indicated phases, as monitored by XRD, during indicated thermal treatment under WGS mixture of Cu6Ce4 (left) and (Cu9Mn1)6Ce4 (right) catalysts. The shift of the fluorite CeO_2 lattice parameter with respect to the initial value is also represented (values in the right axis). Top: evolution of indicated gases during the treatment under the WGS mixture.

Figure 6. Top: evolution of the indicated phases and shift of the fluorite CeO_2 lattice parameter with respect to the initial value (right axis), as monitored by XRD, during treatment under CO-TPR conditions of Cu6Ce4. Middle: the same for (Cu9Mn1)6Ce4. Bottom: evolution of m/e = 44 MS signal corresponding to CO_2 during the CO-TPR run for the indicated catalysts.

Figure 7. Top: XANES spectra of (Cu9Mn1)6Ce4 at the Cu K-edge under WGS mixture at the indicated temperatures and reference samples. Middle: EXAFS radial distribution function obtained from corresponding Cu K-edge spectra for (Cu9Mn1)6Ce4 under WGS mixture at the indicated temperatures and reference samples. Bottom: evolution of copper states under the WGS mixture as obtained from analysis of the Cu K-edge XANES spectra.

Figure 1

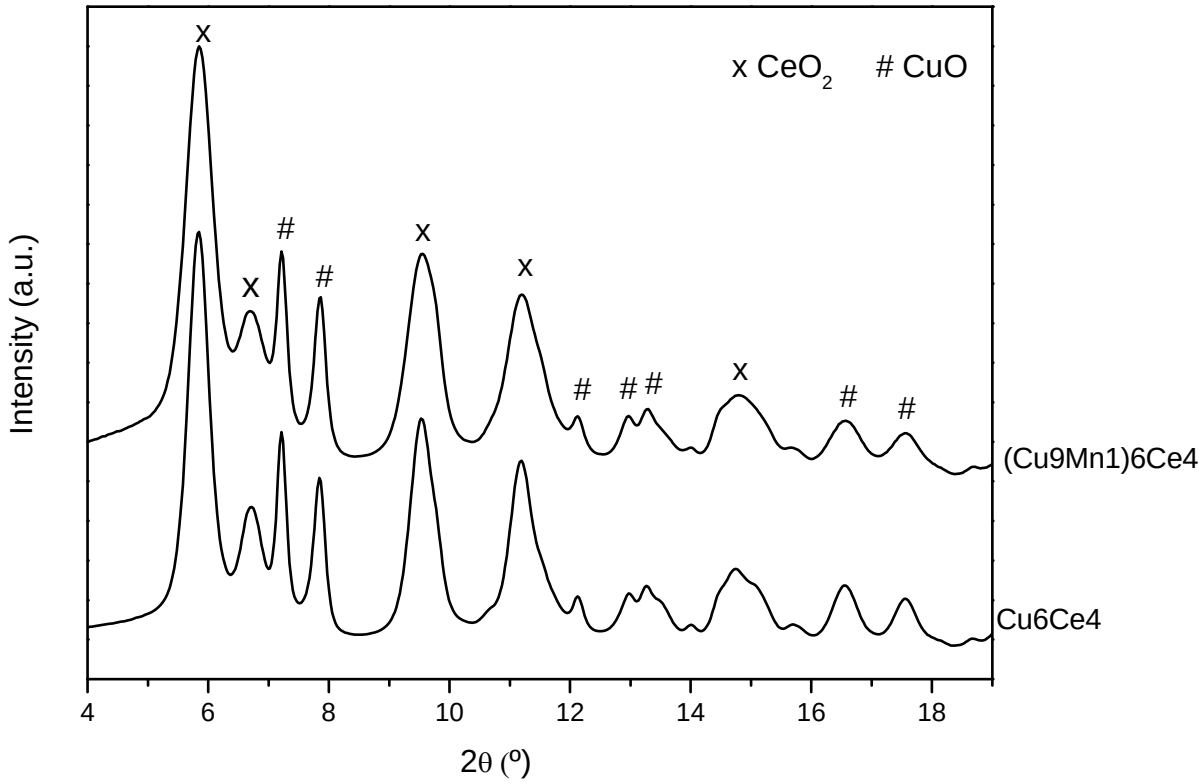
x CeO2 # CuO
Intensity (a.u.)
2θ (º)
(Cu9Mn1)6Ce4
Cu6Ce4
4
6
8
10
12
14
16
18

Figure 2

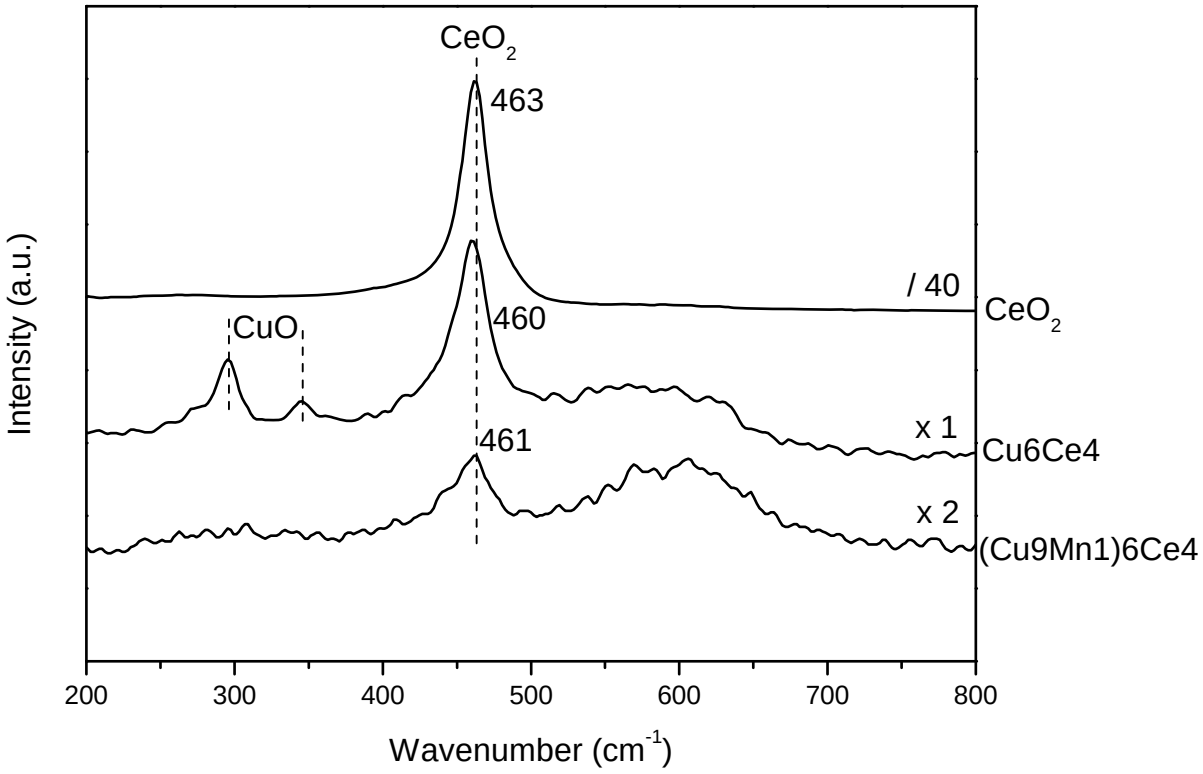
CeO2
463
/ 40
CeO2
CuO
460
x 1
Cu6Ce4
461
x 2
(Cu9Mn1)6Ce4
Intensity (a.u.)
200
300
400
500
600
700
800
Wavenumber (cm-1)

Figure 3

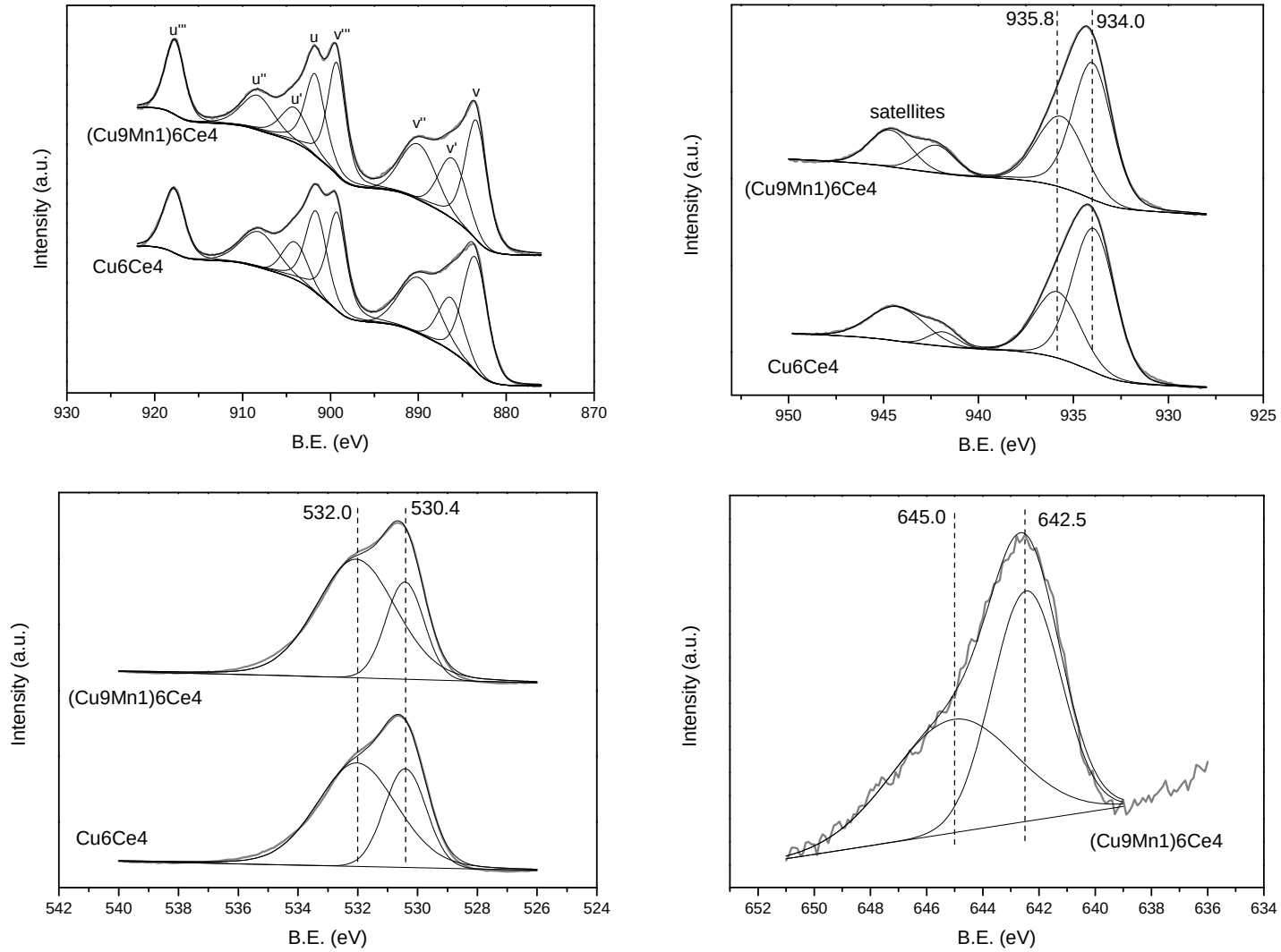
u'''
u''
u
v'''
u'
v''
v
v'
(Cu9Mn1)6Ce4
Cu6Ce4
Intensity (a.u.)
930
920
910
900
890
880
870
B.E. (eV)
935.8
934.0
satellites
(Cu9Mn1)6Ce4
Cu6Ce4
Intensity (a.u.)
950
945
940
935
930
925
B.E. (eV)
532.0
530.4
(Cu9Mn1)6Ce4
Cu6Ce4
Intensity (a.u.)
542
540
538
536
534
532
530
528
526
524
B.E. (eV)
645.0
642.5
(Cu9Mn1)6Ce4
Intensity (a.u.)
652
650
648
646
644
642
640
638
636
634
B.E. (eV)

Figure 4

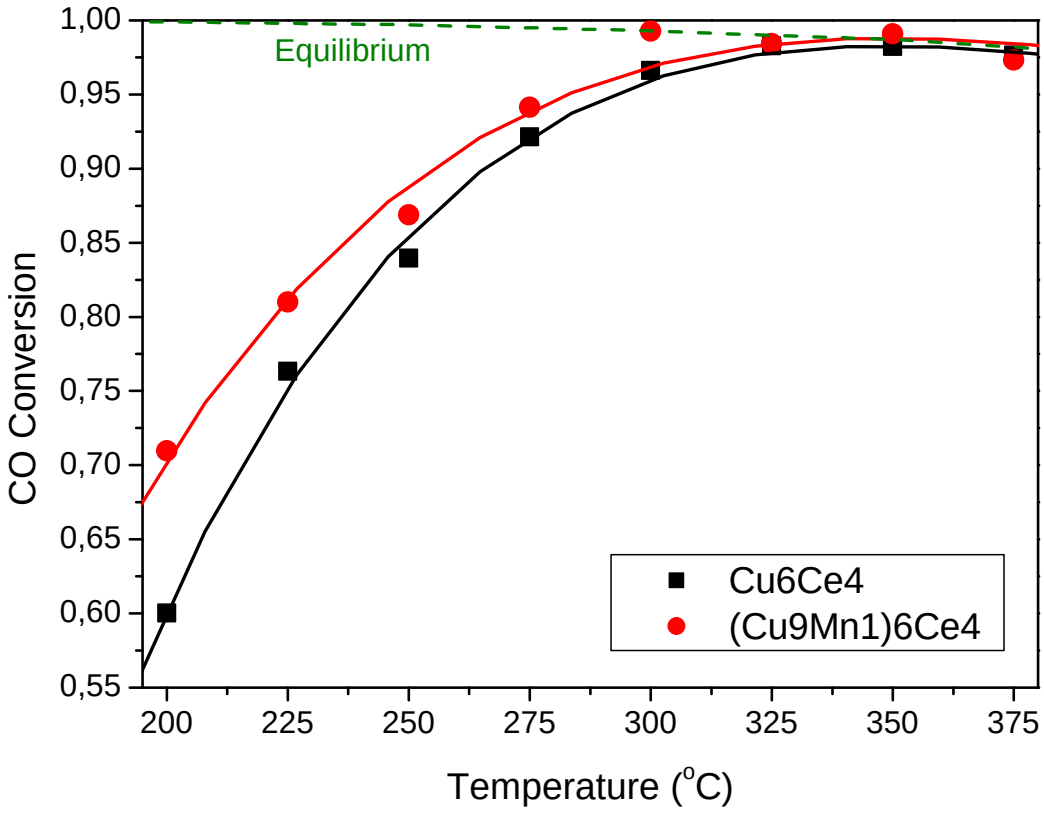
1,00
0,95
0,90
0,85
0,80
0,75
0,70
0,65
0,60
0,55
CO Conversion
Equilibrium
Cu6Ce4
(Cu9Mn1)6Ce4
200
225
250
275
300
325
350
375
Temperature (°C)

Figure 5

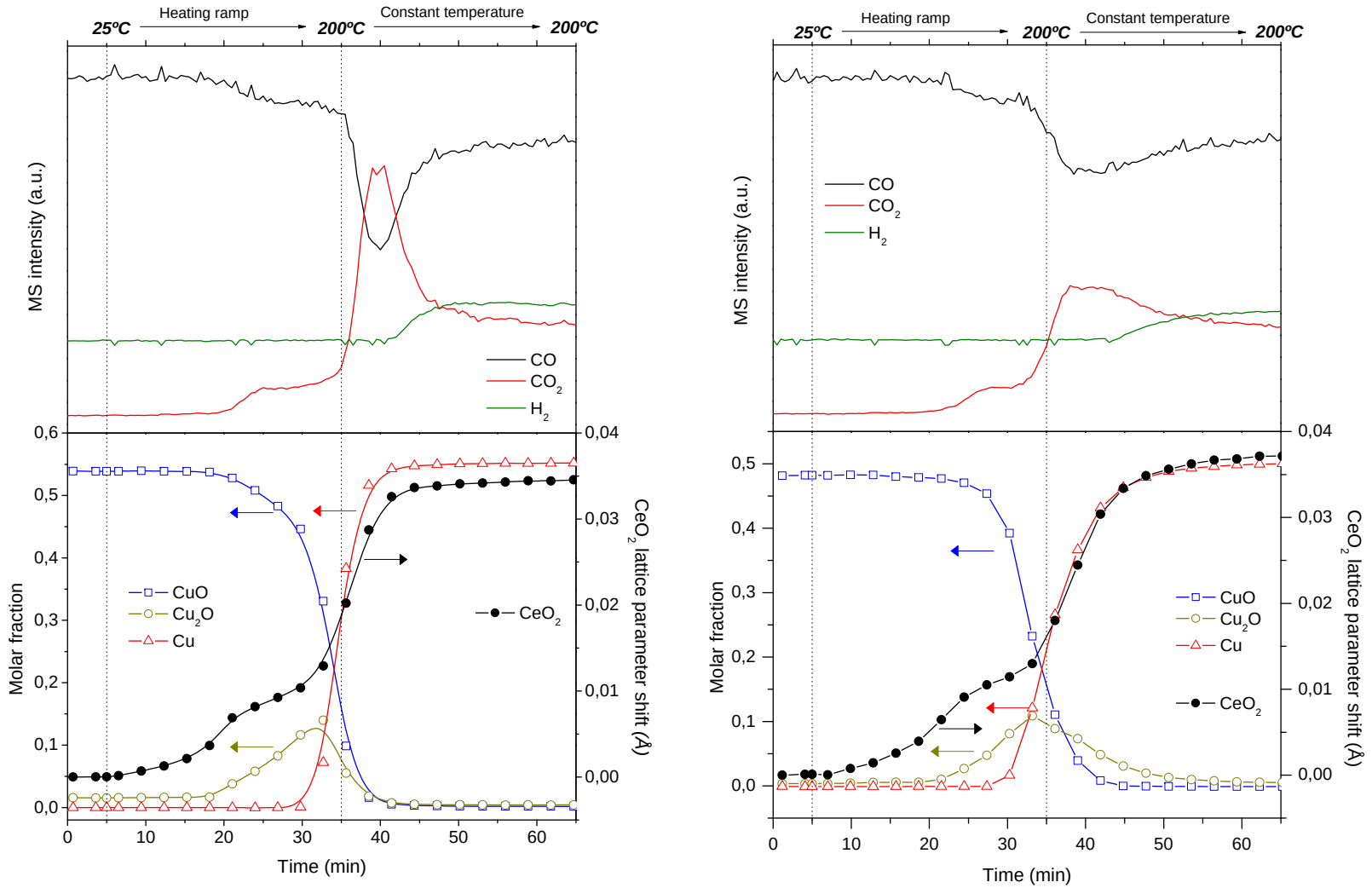
25ºC
Heating ramp
200ºC
Constant temperature
200ºC
MS intensity (a.u.)
CO
CO2
H2
Molar fraction
CuO
Cu2O
Cu
CeO2
CeO2 lattice parameter shift (Å)
Time (min)

Figure 6

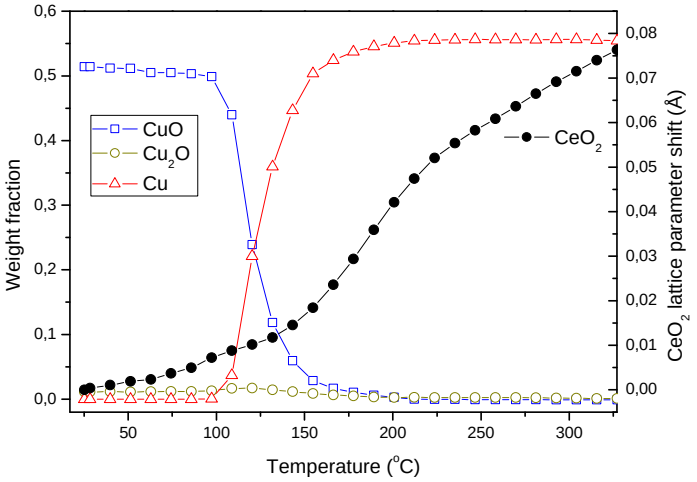
Weight fraction
CeO2 lattice parameter shift (Å)
Temperature (°C)
CuO
Cu2O
Cu
CeO2

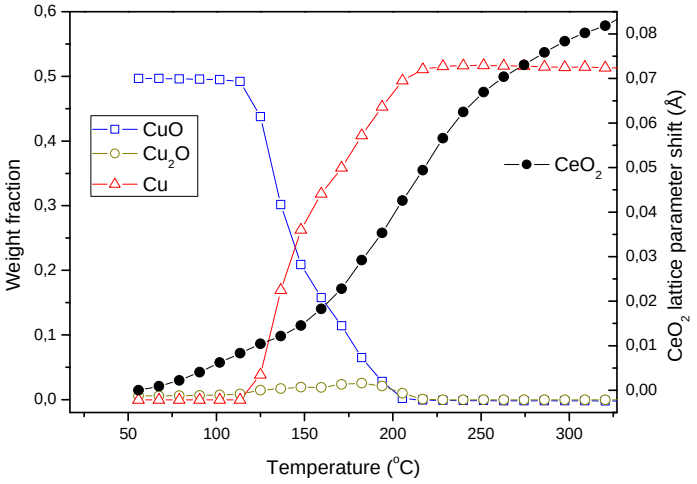
Weight fraction
CeO2 lattice parameter shift (Å)
Temperature (°C)
CuO
Cu2O
Cu
CeO2

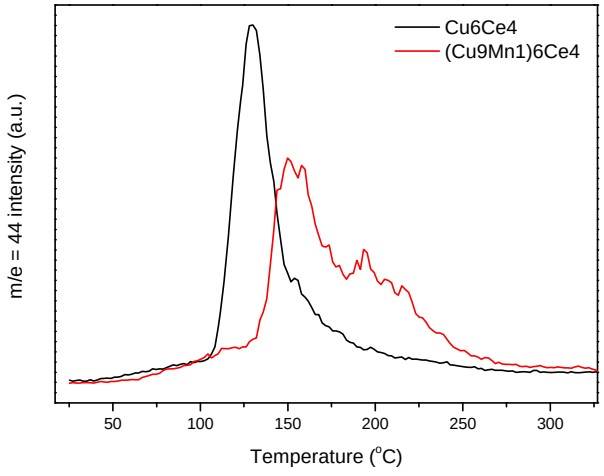
m/e = 44 intensity (a.u.)
Temperature (°C)
Cu6Ce4
(Cu9Mn1)6Ce4

Figure 7

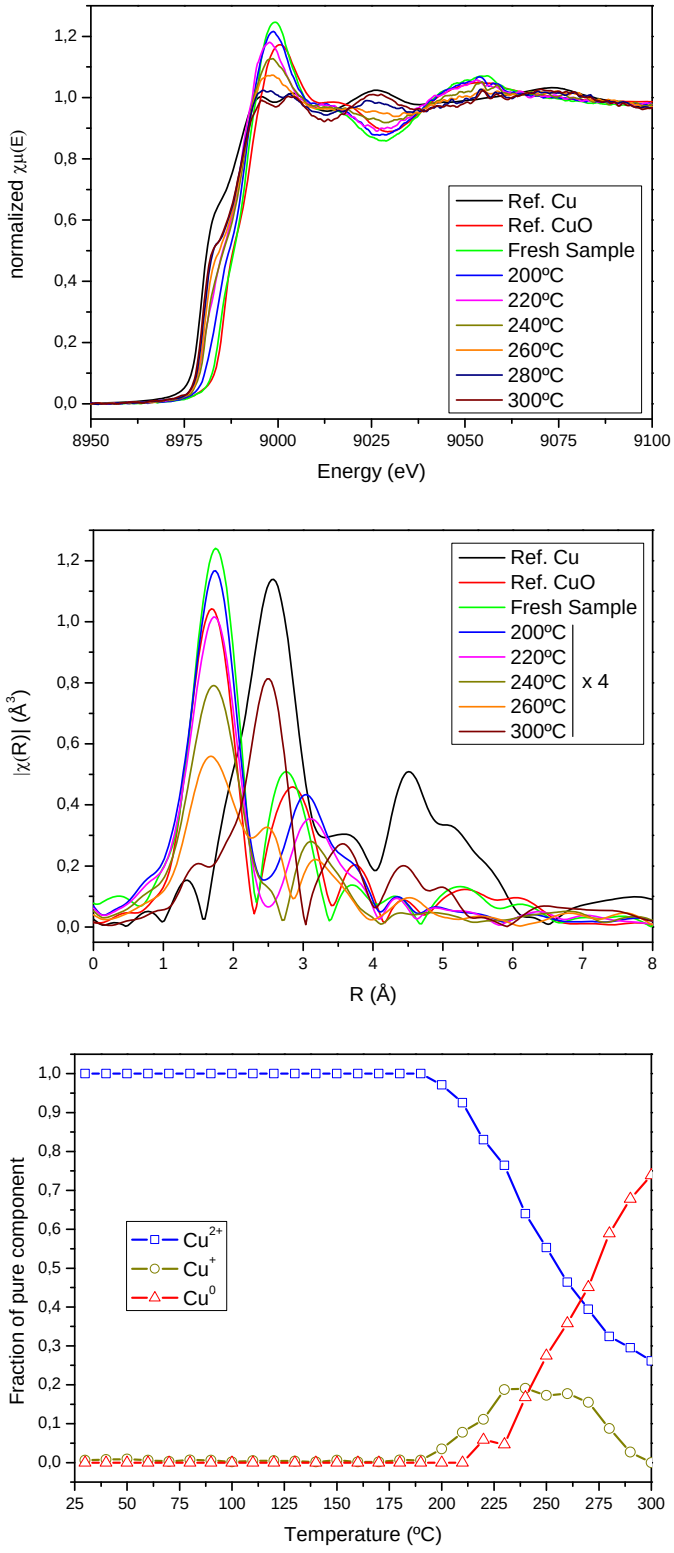
normalized χμ(E)
Energy (eV)
Ref. Cu
Ref. CuO
Fresh Sample
200ºC
220ºC
240ºC
260ºC
280ºC
300ºC
|χ(R)| (Å^3)
R (Å)
x 4
Fraction of pure component
Temperature (ºC)
Cu^{2+}
Cu^{+}
Cu^{0}